Monthly Notices
of the
ROYAL ASTRONOMICAL SOCIETY

MNRAS **481,** 2470–2478 (2018)
Advance Access publication 2018 September 6

doi:10.1093/mnras/sty2447

A rapid occultation event in NGC 3227

T. J. Turner [1,2★] J. N. Reeves,[2] V. Braito [2,3] A. Lobban,[4] S. Kraemer[5] and L. Miller[6]

[1]*Department of Physics, University of Maryland Baltimore County, Baltimore, MD 21250, USA*
[2]*Center for Space Science and Technology, University of Maryland Baltimore County, 1000 Hilltop Circle, Baltimore, MD 21250, USA*
[3]*INAF – Osservatorio Astronomico di Brera, Via Bianchi 46 I-23807 Merate (LC), Italy*
[4]*Astrophysics Group, School of Physical and Geographical Sciences, Keele University, Keele, Staffordshire ST5 5BG, UK*
[5]*The Catholic University of America, Washington, DC 20064, USA*
[6]*Department of Physics, University of Oxford, Keble Road, Oxford, OX1 3RH, UK*

Accepted 2018 September 3. Received 2018 August 31; in original form 2018 July 23

ABSTRACT

NGC 3227 exhibits rapid flux and spectral variability in the X-ray band. To understand this behaviour, we conducted a coordinated observing campaign using 320 ks of *XMM–Newton* exposures together with 160 ks of overlapping *NuSTAR* observations, spanning a month. Here, we present a rapid variability event that occurs toward the end of the campaign. The spectral hardening event is accompanied by a change in the depth of an unresolved transition array (UTA), whose time-dependent behaviour is resolved using the RGS data. This UTA fingerprint allows us to identify this as a transit event, where a clump of gas having $N_{\rm H} \sim 5 \times 10^{22}$ atoms cm^{-2}, log $\xi \sim 2$ occults ∼60 per cent of the continuum photons over the course of approximately a day. This occulting gas is likely associated with clouds in the inner broad-line region. An additional zone of gas with lower column and higher ionization, matches the outflow velocity of the variable zone, and may represent transmission through the cloud limb.

Key words: galaxies: active – galaxies: individual: NGC 3227 – galaxies: Seyfert – X-rays: galaxies.

1 INTRODUCTION

Detailed measurement of X-ray spectral features, especially using grating data, has revealed a complex, multizoned outflowing X-ray reprocessor that shapes the observed properties of Active Galactic Nuclei (AGNs; Blustin et al. 2005). X-ray observations are particularly valuable for understanding the mass and energy carried by the gas, as they can trace the entire radial extent of the nuclear outflow. Fluctuations in the intrinsic X-ray continuum will reverberate from the reprocessing gas, which may show a delayed scattered X-ray signal or a change in gas ionization state in response to the continuum. The detectability of these responses depends on many factors, including the degree of continuum variation, initial state of the gas, and the orientation of the system. For cases where the plane of the reprocessing gas lies predominantly in our line of sight, one might expect to see occultation and uncovering events if the reprocessor is clumpy, such as in the form of a cloud ensemble.

The X-ray reprocessing zones have outflow velocities that range from hundreds of km s^{-1} to a fraction of c (Gofford et al. 2013; Tombesi et al. 2013) and may be phenomenologically linked to the outflows observed in the UV and optical spectra of these sources. The gas feeding the flow may originate from the surface of the accretion disc, the optical broad line clouds, the putative obscuring torus or may include contributions from all of these.

For such complex systems, simultaneous consideration of spectral and timing properties is necessary to disentangle the various modes of behaviour and elucidate the location, physical state, mass and energy carried in the reprocessing gas. Long time-scale absorption events have been observed in sources such as NGC 3783, whose variability reveals a clumpy X-ray reprocessing wind (e.g. Mehdipour et al. 2017) located at the outer part of the optical broad-line region (BLR). The X-ray light curves of MCG-6-30-15 (McKernan & Yaqoob 1998) and NGC 3516 (Turner et al. 2008) have been captured during dips whose profiles are characteristic of occultation events, also indicative of absorption close to BLR radii. Similar X-ray absorption events have also been found in Mrk 335 (Longinotti et al. 2013), NGC 5548 (Kaastra et al. 2014), and NGC 985 (Ebrero et al. 2016).

X-ray spectral data have been particularly valuable, as they can trace variability in spectral features, such as in the Fe K-band absorption lines as seen in NGC 1365 (Risaliti et al. 2007, 2009) and NGC 3227 (Lamer, Uttley & McHardy 2003) – unambiguous signatures of changes in the line-of-sight opacity on time-scales of days. In the most extensively studied sources, such as NGC 1365 (Braito et al. 2014), NGC 5548 (Cappi et al. 2016), and NGC 3783 (Kaastra et al. 2018) absorption variations are observed across a wide range of time-scales, showing a large radial range for the X-

★ E-mail: tjturner@umbc.edu

ray absorption complex, down to the accretion disc scale (Kaastra et al. 2014). It seems likely that the X-ray reprocessor is composed of zones covering a wide range of radii such that variability result captured depends on the observation specifics convolved with the scale size and physical state of the gas in a particular AGN.

More generally, the characteristic softening of the observed X-ray spectrum in high-flux states is very common in AGN. This behaviour has been successfully modelled as absorption changes, such as variations in the gas covering fraction such that high states contain a greater fraction of direct light than low states (e.g. NGC 3227, Lamer et al. 2003; Mrk 766, Miller et al. 2007; MCG-06-30-16, Miller, Turner & Reeves 2008). In a number of targets, X-ray variability time-scales and fitted ionization parameters have been among measurements used to determine that a significant component of the X-ray reprocessing gas is likely co-incident with the BLR (e.g. Bianchi, Maiolino & Risaliti 2012).

Thus, results to date are building up a new Unified Model for AGN, built around the idea of a cloud ensemble as the obscuring material. A concentration of clouds is suggested to lie close to the equatorial plane of the accretion disc, with an angular distribution that falls off toward the poles (Nenkova, Ivezić & Elitzur 2002; Elitzur & Shlosman 2006; Nenkova et al. 2008). New infrared data yield information on the gas distribution outside of the dust sublimation radius and results generally support a cloud ensemble rather than a simple torus distribution for the gas (e.g. Alonso-Herrero et al. 2011).

NGC 3227 is a Seyfert 1.5 galaxy at $z = 0.003859$, that has shown high unabsorbed (e.g. Lamer et al. 2003) and absorbed low X-ray states in previous X-ray observations (Markowitz et al. 2009; Rivers, Markowitz & Rothschild 2011; Markowitz, Krumpe & Nikutta 2014). A study using *XMM*, *Suzaku,* and *Swift* data (Beuchert et al. 2015) found an outflowing warm absorber that is complex, with signatures from three zones of ionized gas with transit by one inhomogeneous clump of gas linking part of the absorber complex to the location of the optical BLR. Further to this, variations have been observed in the Fe K-shell absorption lines (Gofford et al. 2013) and a so-called negative lag detected in the lag-frequency spectrum, indicating the presence of a significant reverberated signal from reprocessing gas out of the line of sight (De Marco et al. 2013).

Time-resolved absorption events, such as that reported by (Beuchert et al. 2015), are still quite rare. The observation of such in NGC 3227, along with its wide range of observed spectral states motivated the 2016 *XMM*/*NuSTAR* campaign comprising ∼320 ks of *XMM–Newton* time overlapping ∼160 ks of *NuSTAR* observations. The new campaign sampled the source on days to weeks to elucidate the nature of the X-ray reprocessor. In this paper, we present results from a subset of the new data, within which a rapid absorption event was isolated.

In Section 2, we provide details of the observations and data reduction. In Section 3, we present a brief overview of the campaign, showing the source light curve and the hardness ratio behaviour that identifies the time period of particular interest with regard to spectral variability. In Section 4, we develop a spectral model for the source prior to the absorption event. In Section 5, we assess the spectral variability of NGC 3227 from a subset of observations from 2016 December 05–09, using both the RGS and pn spectra to quantify the absorber variability. In Section 6, we discuss the parameters drawn from our results and attempt to place the relative location of the absorbing gas.

Table 1. Observation Log.

Date	Observation ID	Total Exposure	Flux 2–10 keV
XMM			
2016-11-09 12:51:03	0782520201	92.0	3.24
2016-11-25 10:25:35	0782520301	74.0	2.59
2016-11-29 13:10:38	0782520401	84.0	3.12
2016-12-01 09:58:49	0782520501	87.0	3.65
2016-12-05 09:42:23	**0782520601**	**86.6**	**4.10**
2016-12-09 09:24:49	**0782520701**	**87.9**	**3.78**
NuSTAR			10–50 keV
2016-11-09 13:16:08	60202002002	49.8	6.99
2016-11-25 09:26:08	60202002004	42.5	5.99
2016-11-29 16:31:08	60202002006	39.7	6.37
2016-12-01 10:31:08	60202002008	41.8	7.47
2016-12-05 09:31:08	**60202002010**	**40.9**	**7.79**
2016-12-09 08:36:08	**60202002012**	**39.2**	**7.56**

Note: Observed fluxes are given in units 10^{-11} erg cm^{-2} s^{-1} based on the *XMM* pn and the mean FPM data. Bold face type denotes the sequences presented in this paper.

2 OBSERVATIONS

2.1 *XMM–Newton*

XMM–Newton (hereafter *XMM*) conducted six observations of NGC 3227 over the period 2016 November 09–December 09 as part of a coordinated *XMM*/*NuSTAR* campaign). The *XMM* observations were spaced over time-scales of days to weeks to sample the source's different flux states, with exposures between 74 and 92 ks (Lobban et al. 2018, in prep). Table 1 gives a summary of the observations. The 2016 December 09 data from OBSID 0782520701 captured a rapid absorption event (Figs 1 and 2). Here we present the *XMM* spectral data that allow a parametrization of the event. To set the baseline for the spectral change, we also include spectral analysis of the preceding data from 2016 December 05 (OBSID 0782520601), along with the overlapping *NuSTAR* data.

All the *XMM* observations were performed in Small Window mode, with the medium filter applied. All data were processed using SAS v16.1.0 and HEASOFT v6.23 software and the data reduction and extraction is described in full in a companion paper by Lobban et al. (2018, in prep). Each observation was filtered for high background, which did not affect the subset of observations presented here. We extracted the EPIC pn source and background spectra using a circular region with a radius of 35 arcsec and two circular regions with a radius of 28 arcsec, respectively. After cleaning, the December 05 (601) and December 09 (701) *XMM* event files yielded exposures of ∼60 ks and 53 ks, respectively, with mean 0.5–10.0 keV count rates of 14.5 and 10.3 source ct/s, in the pn and 0.36 and 0.23 ct/s, respectively over 0.5–2.0 keV in the summed RGS 1 and 2 spectra for the two dates. We generated the response matrices and the ancillary response files at the source position using the SAS tasks *arfgen* and *rmfgen* and the latest calibration available. The pn spectrum was binned to a minimum of 50 counts per energy bin: the binned data maintained sampling finer than the spectral resolution of the pn. The background rate was <1 per cent of the net source rate in the pn.

The *XMM* RGS1 and RGS2 data were reduced with the standard SAS task RGSPROC, where we filtered for high background time intervals applying a threshold of 0.2 cts s^{-1} on the background event files. We then combined the RGS1 and RGS2 spectra with the

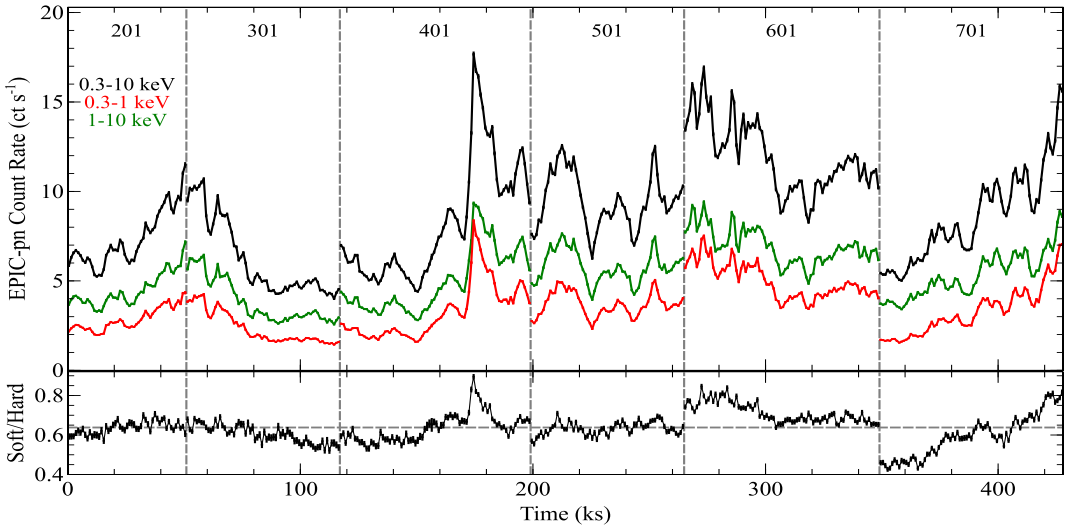

Figure 1. Upper panel: the *XMM–Newton* EPIC-pn light curve of NGC 3227 in 1 ks bins across all six observations from 2016. The broad-band light curve (0.3–10 keV) is shown in black while soft (0.3–1 keV) and hard (1–10 keV) bands are shown in red and green, respectively. Lower panel: the evolution of the 'softness ratio' (i.e. soft/hard) over the course of the campaign.

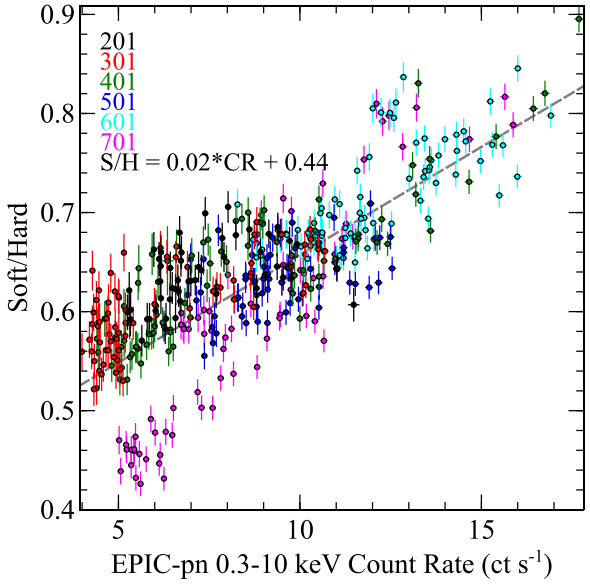

Figure 2. The 'softness ratio' (i.e. soft/hard) of NGC 3227 using the EPIC-pn data in 1 ks bins. The six observations are shown in different colours – chronologically: black, red, green, blue, cyan, and magenta. The soft and hard bands are defined as 0.3–1 and 1–10 keV, respectively. The grey dashed line shows a linear best-fitting model with a slope of 0.02 and a positive offset of 0.44. Note that observation 701 (magenta) lies off the best-fitting slope, hinting at unusual spectral behaviour during this time.

SAS task RGSCOMBINE, after checking that the RGS1 and RGS2 spectra were in good agreement. We then extracted the background-corrected light curves using the SAS task *rgslccorr* for the total RGS band adopting a binsize of 1 ks. We inspected the light curves obtained for each RGS (considering only the first order data) as well as for the whole RGS (i.e. combining both the RGS1 and RGS2) and we found that during the December 09 observation NGC 3227 clearly varied also in the RGS band. We then extracted and combined the RGS1 and RGS2 spectra for each of the time intervals that we defined (see Section 3). The RGS spectra collected during the subslices of 0782520701 (see Section 3) received a constant spectral binning, $\Delta\lambda = 0.1$ Å, while for the averaged RGS1 and 2 spectra from each of sequences 0782520601 and 0782520701 received a finer binning, ($\Delta\lambda = 0.03$ Å). The background comprised < 7 per cent of the net source rate in the RGS data over 0.5–2 keV; note that even at the finer binning each of the RGS, the spectral bins have more than 20 counts per bin, which allow us to use the χ^2 statistic for the spectral fitting.

2.2 *NuSTAR*

NuSTAR carries two coaligned telescopes containing Focal Plane Modules A and B (FPMA, FPMB; Harrison et al. 2013) covering a useful bandpass of $\sim 3 - 80$ keV for AGN. *NuSTAR* observed NGC 3227 during 2016 November 09–December 09 covering the *XMM* baseline with overlapping exposures occurring on the same days, as required for the joint observational campaign with *XMM*. An additional observation was made on 2017 Januaryf 21 to coordinate with a GTO observation performed using *Chandra* HETG. Those data are not included here as they occurred approximately six weeks after the end of the nominal campaign, but they will be included in a future paper. The *NuSTAR* OBSID identifiers for the exposures from 2016 December 05 and December 09 presented here are 60202002010 and 60202002012.

Event files were created through the NUPIPELINE task, calibrated with files from CALDB 20180419 and cleaned applying the standard screening criteria, where we filtered for the passages through the SAA setting the mode to 'optimized' in NUCALSAA. This yields net exposures of ∼40 ks per focal plane module. For each of the Focal Plane Module (FPMA and FPMB) the source spectra were extracted from a circular region with a radius of 70 arcsec, while the background spectra were extracted from a circular region with a 75 arcsec radius located on the same detector. NuSTAR source spectra were binned to 100 counts per spectral channel, maintaining a sampling that is finer than the spectral resolution of the instruments. (In some of the plots the data are binned more coarsely than allowed in the fit, for visual clarity.)

During 2016 December 05 FPMA gave a mean source count rate over 3–50 keV of 1.18 ± 0.005 ct/s, FPMB gave 1.12 ± 0.005

ct/s. December 09 FPMA yielded 1.14 ± 0.007, FPMB gave 1.06 ± 0.005; the background level was ∼1 per cent of the total count rate for both dates and modules. These rates correspond to fluxes $\sim 4.0 \times 10^{-11}$ erg cm^{-2} s^{-1} in the- 2–10 keV band and $\sim 7.5 \times 10^{-11}$ erg cm^{-2} s^{-1} in the 10–50 keV band, for both epochs.

There is a small calibration offset recommended to be allowed between FPMA and FPMB and so a constant component was allowed in all models, constrained to a range of 0.9–1.1 for the cross-normalization constant between the pn and *NuSTAR* detectors.

2.3 General Considerations

Spectra are analysed with XSPEC v12.9.1m. We used data over 0.5–10 keV for the pn, 0.4–2.0 keV for RGS, and 3–70 keV for *NuSTAR*. All models included the Galactic line-of-sight absorption, $N_{\rm H,Gal} = 2.0 \times 10^{20}$ cm^{-2} (Dickey & Lockman 1990), parametrized using TBABS. All model components were adjusted to be at the redshift of the host galaxy, except for the Galactic absorption. For the ionized absorber model tables, we used version 2.41 of the XSTAR code (Kallman & Bautista 2001; Kallman et al. 2004), assuming the abundances of Grevesse & Sauval (1998). XSTAR models the absorbing gas as thin slabs, with parameters of atomic column density and ionization parameter ξ, defined as

$$\xi = \frac{L_{\rm ion}}{n_{\rm e} r^2}$$

that has units erg cm s^{-1} and where $L_{\rm ion}$ is the ionizing luminosity between 1 and 1000 Rydbergs, n_e is the gas density in cm^{-3} and r is the radial distance (cm) of the absorbing gas from the central continuum source. The spectral energy distribution was taken to be a simple power law with $\Gamma = 2$. The turbulent velocity was taken as $\sigma = 300$ km s^{-1}. (The turbulent velocity widths are consistent with the upper limits on the narrow absorption lines seen later in the RGS data.)

In the fits, unless otherwise stated, parameters are quoted in the rest frame of the source and errors are at the 90 per cent confidence level for one interesting parameter ($\Delta\chi^2 = 2.706$).

3 INITIAL OVERVIEW OF THE CAMPAIGN

Light curves were constructed and the individual sequences from the campaign concatenated together (to remove the gaps, for visual clarity regarding the source behaviour). NGC 3227 shows strong X-ray variability across the observation set (Fig. 1), across the bandpass of the *XMM* data. Initial inspection of the data revealed the source spectrum to be hard in the low-flux states, and soft in the high states, as observed previously for local Seyfert galaxies (e.g. Miller et al. 2010). Consideration of the hardness ratio behaviour allowed the isolation of an epoch of unusual spectral behaviour, i.e. an abrupt hardening of the source spectrum at the start of OBSID 0782520701, the exposure from 2016 December 09, which was the last observation of the 2016 campaign. Fig. 2 shows the significant hardening and illustrates how that is different in characteristics to previous sequences in this campaign, even those where NGC 3227 occupied a similar flux state.

To further our understanding, we constructed a light curve from the *NuSTAR* data over the 10–50 keV band, and compared this with the *XMM* pn and RGS light curves over the December 09 data (note that there was a slight offset between the start times of the *NuSTAR* and *XMM* segments of data). This comparison showed the 10–50 keV band to be steady in flux, while the lower energy flux levels varied (Fig. 3). Based upon the variability of flux below 10 keV,

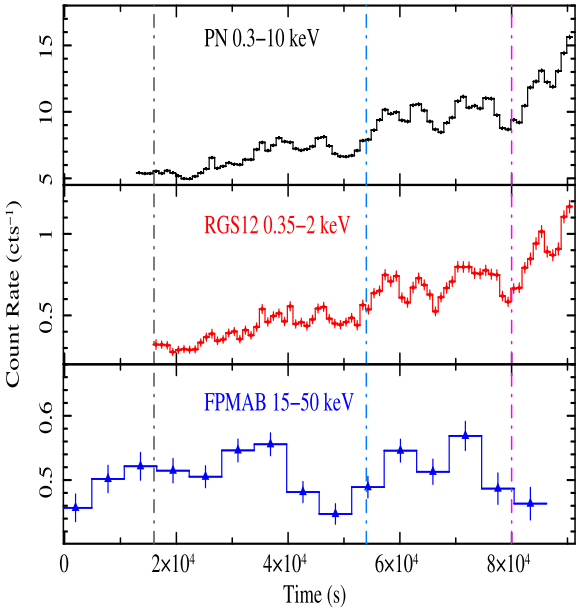

Figure 3. The light curves for *XMM* RGS and pn instruments, using 1000 s time bins and the overlapping *NuSTAR* data from December 09, binned to the *NuSTAR* orbit time-scale (∼5800 s). The vertical dash–dotted lines show the time selections: the first interval is discarded as it contains only *NuSTAR* data without *XMM*, the second interval is denoted slice A, third is slice B, and the final slice is C.

we split the data from December 09 into three intervals to sample the source spectrum as the flux changed. The time intervals chosen are shown in Fig. 3 and denoted by the vertical dash–dotted lines. We subdivided the spectral data and examined the shape changes across the three time slices chosen: Slice A was the first segment of the December 09 data and had an exposure of 27 ks, slice B was the middle segment with an exposure 17 ks, and slice 3 the final segment with just 6 ks (although being the highest flux state this had adequate counts for analysis). These slices will be considered in the spectral variability analysis presented in Section 5.

4 CHARACTERIZATION OF THE BASELINE X-RAY SPECTRUM

Motivated by the sudden change in spectral behaviour exhibited on December 09, we proceeded to parametrize the X-ray form during 2016 December 05, to establish the spectral baseline immediately prior to the hardening event.

4.1 Characterizing December 05 RGS data

We began with a detailed analysis of the RGS spectral data from December 05, to fully characterize the warm absorber complex. Owing to the narrow bandpass of the RGS and the complexity of the absorbing gas transmission profile, it is not possible to also determine the underlying spectral continuum from those data. We therefore assumed a photon index of 1.8 and allowed in the fit a blackbody component (that improved the fit from $\chi^2 = 1316/835$ d.o.f. to $\chi^2 = 1033/833$ d.o.f. in the final best fit) whose temperature was $kT = 90$ eV: these values were obtained from a fit to the *XMM* pn and *NuSTAR* data and together they model the underlying continuum. We return to the pn fit in the next section.

The RGS spectrum shows numerous absorption features, and some emission lines, covering a wide range of ionization states of

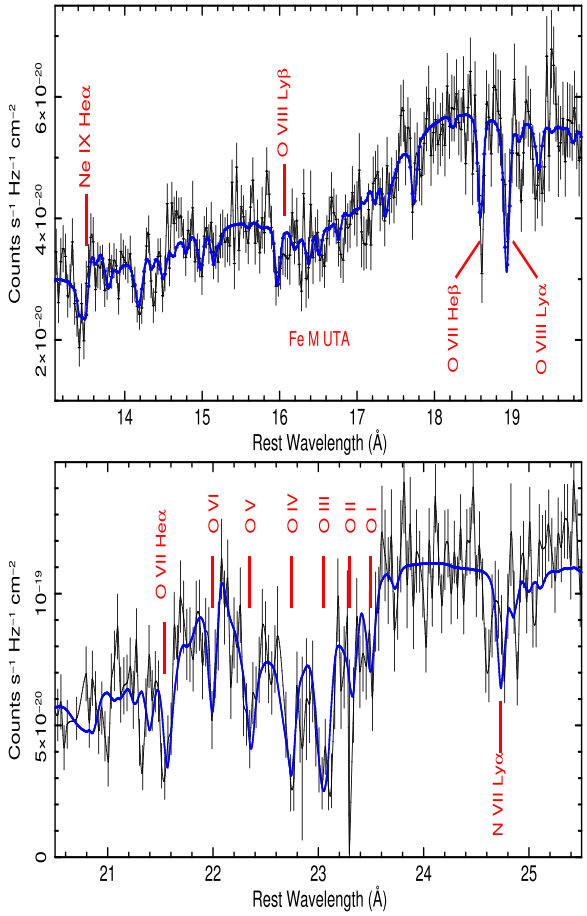

Figure 4. A detailed fit to the RGS data from December 05. Black denotes the summed RGS data and the blue line represents the total model.

Table 2. RGS fit to 2016 Dec 05: Absorption Complex.

Zone	$N_{\rm H}$ $\times 10^{21}$ cm^{-2}	Log ξ	Velocity km s^{-1}
1	$2.07^{+0.17}_{-0.16}$	$-0.63^{+0.06}_{-0.57}$	-157^{+44}_{-46}
2 (UTA)	$0.83^{+0.27}_{-0.19}$	$1.39^{+0.09}_{-0.11}$	-798^{+47}_{-61}
3	$4.42^{+1.14}_{-0.95}$	$2.85^{+0.13}_{-0.09}$	-792^{+52}_{-62}

material. It was necessary to include three XSTAR zones of ionized gas in the model, to adequately model these data. The gas zones showed no evidence for partial covering in the RGS data and so were all assumed to fully cover the source.

The spectral data from the combined RGS gratings are shown in Fig. 4. All of the warm absorber zones have column densities in the range 10^{21}–10^{22} atoms cm^{-2} and cover a wide range of ionization (Table 2). Zone 1 is of relatively low ionization (Table 2) and is responsible for the slew of inner K-shell absorption lines from O I–VI between 20–25 Å whose wavelengths indicate a low bulk outflow velocity $\sim$150 km s^{-1} for this gas. Zone 2 most notably shows a broad signature of Fe M-shell absorption, in an unresolved transition array (UTA) centred between 16–17 Å from gas outflowing at $\sim$800 km s^{-1}. Zone 3 has strong absorption lines from highly ionized species, such as the H-like lines from N VII Ly α, OVIII Lyman α and Lyman β. This zone shows the same outflow velocity as Zone 2.

The fit left significant positive residuals around $\sim$ 18.4 Å (0.674 keV), where an O VIII Ly α emission line is expected, and so we added a broad Gaussian line component to the fit to account for this. Excess emission is also associated with the O VII triplet near 22 Å, where we included a weak narrow component corresponding to the forbidden line and a broader emission component that could correspond to a blend of line emission from the intercombination and resonance line components. He-like emission is also present at 13.6 Å (0.91 keV), likely from Ne IX. This final fit gave $\chi^2 = 1033/833$ d.o.f, compared to 1117/843 without the emission lines. Table 3 shows fitted line energy, widths, velocity width, equivalent width against the local continuum, fitted wavelength, and line identification. A future paper will discuss a detailed fit to the full set of RGS data from this campaign, including the emission line profiles from the mean spectrum.

4.2 Fitting the broad X-ray spectral form for December 05

Having established a model for the signatures of X-ray absorbing gas in the 0.4–2.0 keV band, we then performed a joint fit to the *XMM* pn data from December 05 and simultaneous *NuSTAR* FPM data from 2016 December 05. A model was constructed composed of a power-law continuum modified by passage through ionized gas. As the pn has a lower spectral resolution than the RGS, and the data were taken simultaneously, we fixed the parameters of the three absorbing zones of gas at the values already determined from the RGS fit (Table 2). Reflection was added into the model, based on the presence of a weak ($\sim$70 eV) and narrow Fe Kα emission line at 6.4 keV (Fig. 5). A reflection signature would be expected from gas out of the line of sight, such as might arise from a geometrically thin, optically thick disc subtending 2π steradians to the continuum source. Reflection was parametrized for neutral gas, using the XSPEC model PEXMON and the illuminating photon index was linked to that of the continuum, this component provided a good parametrization of the Fe Kα emission in the spectrum, for an Fe abundance of $1^{+0.3}_{-0.2}$ and reflection fraction $R = 1.07 \pm 0.16$

The best-fitting model to the mean 2015 December 05 spectrum yielded a photon index $\Gamma = 1.84 \pm 0.01$ with a high-energy cut-off $E_{\rm cut} = 309 \pm 73$ keV. The soft part of the spectrum was parametrized by a blackbody component with $kT = 90 \pm 3$ eV, as mentioned previously. This model provided a good fit to the broad X-ray form (Fig. 6), with $\chi^2 = 2215/2035$ d.o.f.

To estimate the ionizing luminosity, we added the *XMM* OM UVW1 filter point to the fit. We accounted for a reddening of E(B−V)=0.18 in the model, using the XSPEC model REDDEN, based upon the results of Crenshaw et al. (2001). Extending the $\Gamma = 2$ powerlaw down to the UVW1 band, we estimate the integrated luminosity over 1–1000 Ryd, after correcting for all intrinsic absorption, to be $L_{\rm ion} \sim 8 \times 10^{42}$ erg cm^{-2} s^{-1}.

5 SPECTRAL VARIABILITY

As the RGS data provide a sensitive test of absorption changes, we first compared the summed RGS data from December 05 (601) with the lowest state taken during December 09, i.e. 701 slice A. Fig. 7 provides an immediate visual confirmation of a significant change in the depth of the UTA feature during the low state comprising slice A, compared to the prior 601 sequence. This requires at least a factor of $\sim$3 increase in the column density of Zone 2 (Table 4), to give an occulting column density of $N_{\rm H} \sim 4.4 \times 10^{21}$ cm^{-2} during slice A of the UTA zone of material having an ionization parameter of log $\xi \sim 1.4$ (Table 2).

Table 3. RGS fit to 2016 Dec 05: Line Emission.

Energy eV	σ eV	σ km s^{-1}	EW eV	wavelength Å	ID
561.4(f)	0.5(f)	–	1 ± 1	22.08 Å	O VII *f*
$564.8^{+2.9}_{-2.4}$	$6.9^{+2.4}_{-1.6}$	3700	7 ± 1	21.95 Å	O VII *r*
$674.7^{+6.9}_{-6.8}$	$21.1^{+6.2}_{-4.4}$	9300	8 ± 2	18.38 Å	O VIII Lyα
$911.0^{+2.4}_{-4.6}$	$1.9^{+7.6}_{-1.9}$	660	4 ± 1	13.61 Å	Ne IX *f*

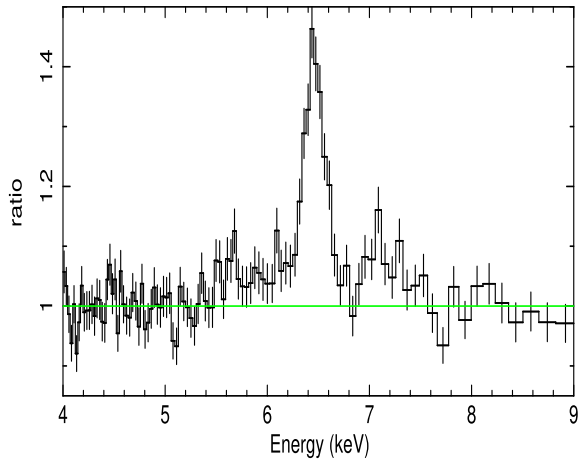

Figure 5. The data ratio in the Fe K band, compared to the local continuum model in pn data for the December 05 data.

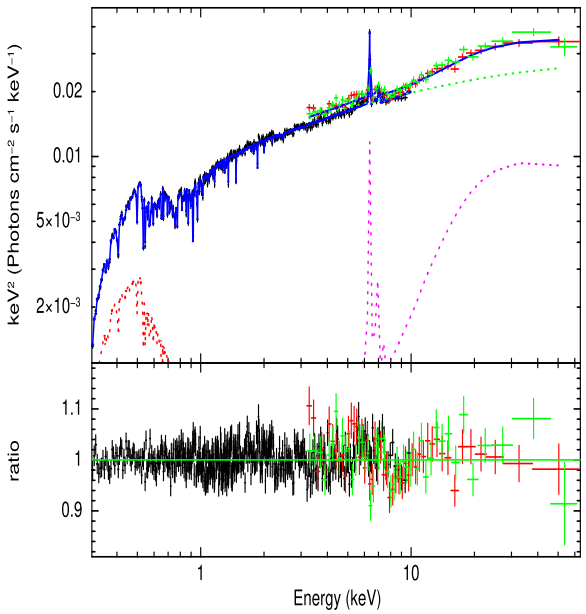

Figure 6. Top: a broad-band fit (top panel) to the *XMM* pn data (black) from December 05 plus the simultaneous *NuSTAR* FPM data (red and green) compared to the total model (solid blue line). Bottom: the data ratio against the model.

We then extended the analysis to compare all three RGS slices from December 09 (701) with the mean (601) spectrum from December 05. Allowing only the column density of Zone 2 to be variable provides sufficient change in the RGS band to account for the spectral variability observed (Fig. 8). The best-fitting parameters for each zone are shown in Table 4, where the column density of the UTA zone increases from $\sim N_{\rm H} = 1.5 \times 10^{21}$ cm^{-2} in the 601 spectrum to a maximum of $N_{\rm H} = 4.4 \times 10^{21}$ cm^{-2} in 701 slice A, which then declines by a factor of 3 within a time-scale of 100 ks by the end of slice C. Thus the observations appear to capture a rapid increase and then decline in the soft X-ray absorber in NGC 3227. Note that in comparison, there is no requirement for any significant variability of either the low-ionization zone 1 or the high-ionization zone 3; all of the absorber variations in the RGS band appear to be associated with the UTA zone 2.

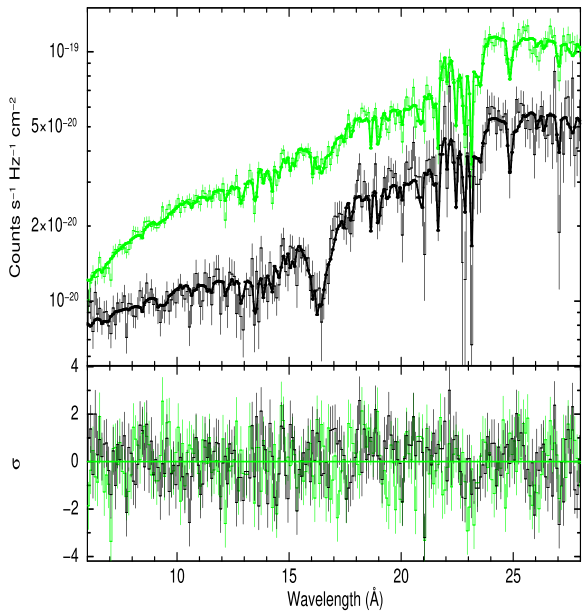

Figure 7. A comparison of the warm absorber during observation of December 05 (green) versus the lowest state slice of December 09 (black). The solid line shows the model documented in Section 5. The variable UTA feature is evident between 16–17 Å.

Table 4. Spectral variability in the RGS band.

Seq	WA Zone 2 $N_{\rm H} \times 10^{21}$ cm^{-2}
601	$1.45^{+0.21}_{-0.28}$
701a	4.43 ± 0.18
701b	3.03 ± 0.27
701c	1.72 ± 0.29

Next, in order to build up a broad-band picture of the spectral variability, we compared the December 05 pn spectral data, with the time-sliced December 09 pn spectra. Inspection of those data shows marked variation in curvature in the few keV regime across the time periods of interest (Fig. 9). In contrast to this, as previously noted,

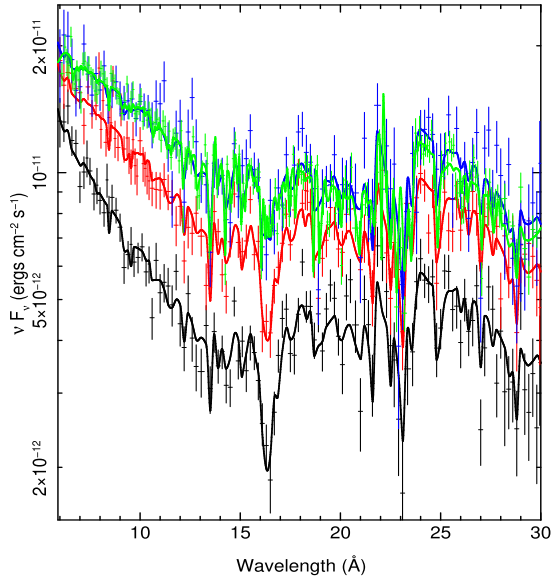

Figure 8. Variability in the warm absorber traced by slicing RGS data from the December 09 data (slice A is black, slice B is red, and slice C is blue) and comparing it to the December 05 data (green).

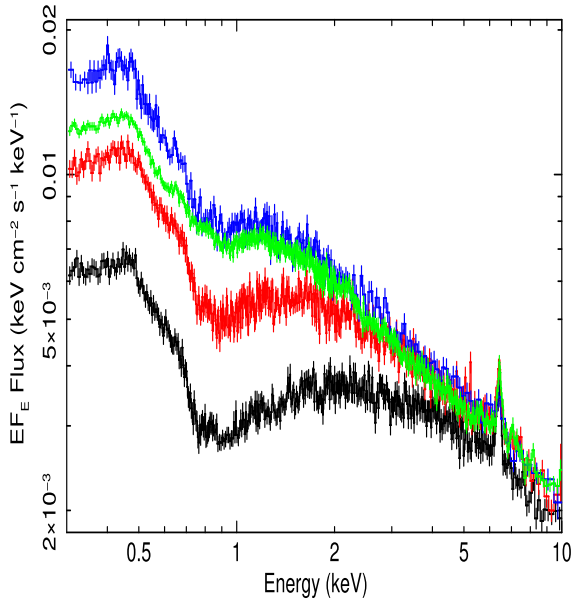

Figure 9. *XMM* pn spectra: the mean spectrum from the December 05 data (green) compared to the slices from December 09, A (black), B (red), and C (blue). The spectra have been unfolded relative to a power law of photon index $\Gamma = 2$.

the source is steady above 10 keV (Fig. 3), i.e. the spectra converge to high energies and no significant spectral variations are seen in any of the *NuSTAR* spectra above 10 keV across either sequence 601 or 701. This allowed us to proceed using a photon index and reflection contribution that are linked (but not frozen) to the same values for the December 05 spectrum and the December 09 spectral slices, although small variations in the normalizations of the continuum

Table 5. Final fit to the X-ray absorption complex after inclusion of the PC Zone.

Zone	$N_{\rm H}$ $\times 10^{21}$ cm^{-2}	Log ξ	Velocity km s^{-1}
1 (full)	$1.79^{+0.16}_{-0.19}$	$-0.65^{+0.06}_{-0.07}$	−157(f)
2 (full – UTA)	1.47 ± 0.23	$1.28^{+0.08}_{-0.13}$	−798 (f)
3 (full)	6.56 ± 0.27	$2.80^{+0.11}_{-0.10}$	−792 (f)
4 (PC)	50.0 ± 2.30	$2.23^{+0.08}_{-0.13}$	−798 (f)

(power law plus blackbody) components were allowed between the slices to account for any intrinsic variability.[1]

After applying the successful RGS model to the time-sliced pn data, we found that a change in column density for the full covering zone 2 is no longer sufficient – as, with the pn data included, we need to explain both the change in depth of the UTA and the strong spectral curvature variations, which is especially noticeable between the December 05 spectrum and slice A from December 09 (Fig. 9). Indeed the fit allowing only the zone 2 fully covering absorber to vary is very poor, with $\chi^2_\nu = 7567/4818$, as the variability of this UTA zone alone is not sufficient on its own to reproduce the strong spectral curvature seen at the start of the 701 pn sequence.

Therefore we added another absorber zone to the model (zone 4), of higher column density, using an XSTAR table configured to partially cover the continuum. Thus, the model form was

$$N_{\rm H,Gal} \times Z_1 \times Z_2 \times Z_3[(1-f) \times (po + ref + bb) + f \times Z_4 \times (po + bb)]$$

where Z 1, 2, 3, and 4 correspond to the ionized absorber zones of Table 5. $N_{\rm H,Gal}$ is the Galactic column represented by TBABS, po is the power law, bb, the blackbody, ref the reflector represented by PEXMON, and f is the covering fraction for zone 4.

The outflow velocity for the partial covering (or 'PC') zone 4 (that is not determinable from the lower resolution pn data) was assumed to be equal to that of zone 2 determined from the RGS spectra (and which is also equal to that of Zone 3). The fit yielded provided a good model to all the pn spectra, with $\chi^2 = 5346/4811$ d.o.f. The PC Zone was found to have $N_{\rm H(PC)} = 5.00^{+0.31}_{-0.06} \times 10^{22}$ cm^{-2} and log $\xi = 2.22^{+0.04}_{-0.04}$. Here we allowed variations in the covering fraction of the PC zone to account for the opacity changes across sequences 601 and 701. The PC Zone is also a UTA producing zone, i.e. it gives significant opacity in the 0.7–0.8 keV regime at the UTA, as can be seen in Fig. 10 (blue curve), as well as producing significant spectral curvature in the soft X-ray band.

Thus the change in covering of the PC zone can simultaneously account for the increase in the soft X-ray spectral curvature of slice A and the increase in strength of the UTA feature, without recourse to additional changes in the column of the full covering zone 2. The column densities and ionization parameters of the full covering zones were therefore linked between slices for the final fit and the outflow velocities were frozen at the values derived from the RGS analysis (see Table 5 for final values). The covering changes of zone 4, that are all we require to explain the absorption event, are shown in Table 6.

[1]Small changes in the blackbody flux were measured at the level of $\sim \pm 5$ per cent between the slices. As these cannot be degenerate with the absorber changes that are based upon strong absorption lines in the RGS band, these fluctuations are not tabulated.

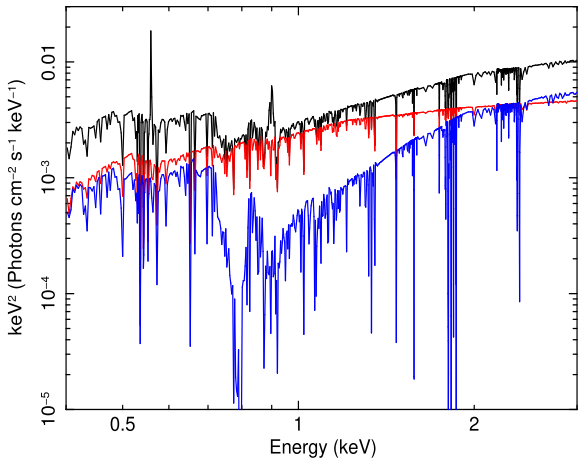

Figure 10. The model for slice A of December 09 data. The blue line is the one absorbed by the heavy pc zone, while the red one is only absorbed by the constant WA (black is the total model including the emission lines). The pc zone is essentially adding in the extra opacity around 0.7–0.8 keV and is thus able to model the increase in strength of the UTA feature as well as the curvature of the continuum.

Fig. 10 shows the final absorber model components for slice A of the December 09 data, where the blue line is the fraction of continuum absorbed by the large-column PC zone, while the red line shows transmission through the constant part of the warm absorber complex (black shows the total spectrum including the emission lines). The UTA is evident in the PC zone, and we note that there is absorption from a blend of O VII–VIII edges present adjacent to that.

6 DISCUSSION

We have analysed new data from simultaneous *XMM* and *NuSTAR* observations of NGC 3227 during 2016 and found a complex X-ray absorber that we have modelled as four zones of ionized gas. Three zones of the absorber are consistent with fully covering the source, while changes in covering fraction of the fourth, PC Zone, account for marked rapid spectral variability.

Following Reeves, Lobban & Pounds (2018), we consider the radial locations of the zones, based upon the fitted spectra and variability time-scales, using the simple relationships that govern the gas behaviour

(i) $\Delta r = v \times \Delta t$ where v is the velocity of the cloud, existing with size Δr and causing an occultation event of duration Δt

(ii) $v^2 = \frac{GM}{r}$ that assume the cloud to be in a Keplerian orbit, at a radial distance r from the black hole of mass M

(iii) $n_e = \frac{\Delta N_H}{\Delta r}$ where n_e is the electron density (equivalent to the particle density), ΔN_H is the change in column density observed, i.e. the integrated column density of the occulting object

(iv) $r^2 = \frac{L_{ion}}{n_e \xi}$ (see Section 2.3 for quantity definitions)

Simultaneous consideration of (i)–(iv) allows algebraic substitutions to be made that negate the need to assume or estimate Δr or n_e, giving

(v) $r^{\frac{5}{2}} = (GM)^{\frac{1}{2}} \frac{L \Delta t}{\Delta N_H \xi}$

NGC 3227 has a black hole of mass $M_{BH} = 5.96^{+1.23}_{-1.36} \times 10^6\,M_\odot$ (Bentz & Katz 2015), with corresponding gravitational radius $r_g \sim 10^{12}$ cm. Considering the change in column density affected by passage of clumps of gas from the PC Zone, we take the time-scale for the occultation event to be $\Delta t \sim 10^5$ s, for the PC Zone the clouds provide $\Delta N_H \sim 5 \times 10^{22}$ cm^{-2} and $\xi \sim 166$. In Section 4.2, we estimated L_{ion} to be $\sim 8 \times 10^{42}$ erg s^{-1}.

Substituting these values into (v) yields $r \sim 6 \times 10^{15}$ cm. Taking this radial estimate, we can estimate the gas transverse velocity from (ii) to be $v \sim 4000$ km s^{-1} and then the cloud size from (i) to be $\Delta r \sim 4 \times 10^{13}$ cm. Following Elitzur & Shlosman (2006) and Beuchert et al. (2015, their equation 14) we can check the viability of this cloud size by examining the upper limit on the size of a cloud that can withstand tidal shearing, finding $\Delta r < 2 \times 10^{13}$ cm. Thus, our cloud size estimate is reasonable. Finally, we can use these derived values in (iii) to obtain an estimate of the gas density for Zone 2, $n_e \sim 10^9$ cm^{-3}.

The optical BLR in this AGN is estimated to exist at a radius of 10–20 light days (Salamanca et al. 1994), i.e. $\sim 2 - 5 \times 10^{16}$ cm. The radial estimate for the PC Zone lies within the BLR, so this gas may comprise or be associated with the clouds of the inner BLR. The time-scale for this variation, of the order of a day, is similar to X-ray absorption variations discovered in some other AGN whose clouds have also been suggested to lie close to the BLR, e.g. NGC 3516 (Turner et al. 2008), NGC 1365 (Braito et al. 2014), NGC 3783 (Mehdipour et al. 2017), and PG1211 + 143 (Reeves et al. 2018). The comparison between NGC 3227 and PG1211 + 143 is especially compelling as in that case the spectral changes are also associated with variations in the UTA feature.

It is interesting that Zone 3, the PC Zone, and Zone 2 all have consistent outflow velocities. A plausible picture is that Zone 2, 3, and the PC zone are all part of the same complex cloud structure. Zone 3 may represent the absorption from the limbs of the PC clouds. Clouds, by their geometry, offer a smaller column density at their limbs than through the centre. The smaller limb-column would naturally suffer a greater degree of ionization by the continuum, consistent with the measurements.

Finally, Zone 1 has a column density $\sim 2 \times 10^{21}$ cm^{-2} of cool gas (Table 5) outflowing with a velocity ~ 150 km s^{-1}. The UV continuum of NGC 3227 is heavily reddened (Komossa & Fink 1997) with a column density for the dusty, reddening gas estimated to be $> 2 \times 10^{21}$ cm^{-2} by Kraemer et al. (2000), an estimate that was supported by Crenshaw et al. (2001). The narrow-line region (NLR) gas shows a maximum velocity of ~ 500 km s^{-1} (Fischer et al. 2013) in this source. The radial location of the NLR is $\sim 10^{20}$ cm (Schmitt & Kinney 1996) in NGC 3227, existing outside of the dust sublimation radius (estimated to be $\sim 10^{17}$ cm, Beuchert et al. 2015). The properties of Zone 1 are consistent with arising as part of the NLR gas and in such a picture, this zone would therefore lie outside of the other components of X-ray absorption in NGC 3227.

7 CONCLUSIONS

We have performed detailed time-resolved spectroscopy of a rapid spectral variability event, occurring over approximately one day, toward the end of a month-long monitoring campaign using *XMM–Newton* with *NuSTAR*. RGS data reveal a UTA imprinted on the spectrum by the X-ray absorber complex. An increase in the UTA depth during the source low state on 2016 December 09 identifies the rapid spectral variability event as changes in absorption. The data are consistent with transit of a gas cloud having $N_H \sim 5 \times 10^{22}$ atoms cm^{-2}, log $\xi \sim 2$, whose movement into the line of sight occults 60 per cent of the X-ray continuum photons during the start of the December 09 exposure. The occulting cloud is estimated to exist on the inner edge of the optical BLR, and has an outflow

velocity $\sim$800 km s^{-1}. One of the additional warm absorbing layers matches the outflow velocity of the variable zone, and may represent transmission through the cloud limb.

NGC 3227 is a complex and heavily absorbed source, whose absorption feature variability make it a high priority for examination with the forthcoming micro-calorimeter on The X-ray Imaging and Spectroscopy Mission (XRISM).

ACKNOWLEDGEMENTS

TJT acknowledges National Aeronautics and Space Administration (NASA) grant NNX17AD91G. Valentina Braito acknowledges financial support through NASA grant NNX17AC40G and through the CSST Visiting Scientist Initiative. APL acknowledges support from Science and Technology Facilities Council (STFC) consolidated grant ST/M001040/1. We are grateful to the *XMM* and *NuSTAR* operations teams for performing this campaign and providing software and calibration for the data analysis.

REFERENCES

Alonso-Herrero A. et al., 2011, ApJ, 736, 82
Bentz M. C., Katz S., 2015, PASP, 127, 67
Beuchert T. et al., 2015, A&A, 584, A82
Bianchi S., Maiolino R., Risaliti G., 2012, Adv. Astron., 2012, 782030
Blustin A. J., Page M. J., Fuerst S. V., Branduardi-Raymont G., Ashton C. E., 2005, A&A, 431, 111
Braito V., Reeves J. N., Gofford J., Nardini E., Porquet D., Risaliti G., 2014, ApJ, 795, 87
Cappi M. et al., 2016, A&A, 592, A27
Crenshaw D. M., Kraemer S. B., Bruhweiler F. C., Ruiz J. R., 2001, ApJ, 555, 633
De Marco B., Ponti G., Cappi M., Dadina M., Uttley P., Cackett E. M., Fabian A. C., Miniutti G., 2013, MNRAS, 431, 2441
Dickey J. M., Lockman F. J., 1990, ARA&A, 28, 215
Ebrero J., Kriss G. A., Kaastra J. S., Ely J. C., 2016, A&A, 586, A72
Elitzur M., Shlosman I., 2006, ApJ, 648, L101
Fischer T. C., Crenshaw D. M., Kraemer S. B., Schmitt H. R., 2013, ApJS, 209, 1
Gofford J., Reeves J.N., Tombesi F., Braito V., Turner T.J., Miller L., Cappi M., 2013, MNRAS, 430, 60
Grevesse N., Sauval A. J., 1998, Space Sci. Rev., 85, 161
Harrison F. A. et al., 2013, ApJ, 770, 103
Kaastra J. S. et al., 2014, Science, 345, 64
Kaastra J. S. et al., 2018, preprint (arXiv:1805.03538)
Kallman T., Bautista M., 2001, ApJS, 133, 221
Kallman T. R., Palmeri P., Bautista M. A., Mendoza C., Krolik J. H., 2004, ApJS, 155, 675
Komossa S., Fink H., 1997, A&A, 327, 483
Kraemer S. B., George I. M., Turner T. J., Crenshaw D. M., 2000, ApJ, 535, 53
Lamer G., Uttley P., McHardy I. M., 2003, MNRAS, 342, L41
Longinotti A. L. et al., 2013, ApJ, 766, 104
Markowitz A., Reeves J. N., George I. M., Braito V., Smith R., Vaughan S., Arévalo P., Tombesi F., 2009, ApJ, 691, 922
Markowitz A. G., Krumpe M., Nikutta R., 2014, MNRAS, 439, 1403
McKernan B., Yaqoob T., 1998, ApJ, 501, L29
Mehdipour M. et al., 2017, A&A, 607, A28
Miller L., Turner T. J., Reeves J. N., 2008, A&A, 483, 437
Miller L., Turner T. J., Reeves J. N., George I. M., Kraemer S. B., Wingert B., 2007, A&A, 463, 131
Miller L., Turner T. J., Reeves J. N., Lobban A., Kraemer S. B., Crenshaw D. M., 2010, MNRAS, 403, 196
Nenkova M., Ivezić Ž., Elitzur M., 2002, ApJ, 570, L9
Nenkova M., Sirocky M. M., Ivezić Ž., Elitzur M., 2008, ApJ, 685, 147
Reeves J. N., Lobban A., Pounds K. A., 2018, ApJ, 854, 28
Risaliti G., Elvis M., Fabbiano G., Baldi A., Zezas A., Salvati M., 2007, ApJ, 659, L111
Risaliti G. et al., 2009, MNRAS, 393, L1
Rivers E., Markowitz A., Rothschild R., 2011, ApJS, 193, 3
Salamanca I. et al., 1994, A&A, 282, 742
Schmitt H. R., Kinney A. L., 1996, ApJ, 463, 498
Tombesi F., Cappi M., Reeves J. N., Nemmen R. S., Braito V., Gaspari M., Reynolds C. S., 2013, MNRAS, 430, 1102
Turner T. J., Reeves J. N., Kraemer S. B., Miller L., 2008, A&A, 483, 161

This paper has been typeset from a TEX/LATEX file prepared by the author.